nature communications

Article

https://doi.org/10.1038/s41467-025-63697-4

Hayabusa2 extended mission target asteroid 1998 KY_{26} is smaller and rotating faster than previously known

Received: 13 January 2025

Accepted: 25 August 2025

Check for updates

T. Santana-Ros[1,2] ✉, P. Bartczak[3,4], K. Muinonen[5], A. Rożek[6], T. Müller[7], M. Hirabayashi[8], D. Farnocchia[9], M. Micheli[10], R. E. Cannon[6], M. Brozović[9], O. Hainaut[11], D. Oszkiewicz[4], A. K. Virkki[5], L. A. M. Benner[9], A. Campo Bagatin[1,3], P. G. Benavidez[1,3], A. Cabrera-Lavers[12,13], C. E. Martínez-Vázquez[14] & K. Vivas[15]

Understanding the physical characteristics of small Solar System bodies is important not only for refining formation and evolution models but also for space mission operations. Although several kilometre-sized asteroids have been visited by spacecraft, asteroid 1998 KY_{26}—the final target of Hayabusa2#, the extended mission of the Japan Aerospace Exploration Agency's Hayabusa2 spacecraft—will be the first decametre-scale asteroid to be explored in situ. Its small size and rapid spin place it above the upper limit on the rotation rate, indicating it may differ from previously studied bodies. In this work, we conducted a photometric campaign during 1998 KY_{26}'s close approach to Earth in 2024, revealing a high optical albedo and Xe-type colours. We determine its spin period to be (5.3516 ± 0.0001) minutes—half the period of earlier estimates. Lightcurve inversion produces retrograde pole solutions in both convex and non-convex shape models. Combined with 1998 Goldstone radar data, these results give a diameter of (11 ± 2) m, three times smaller than previously derived values. The derived cohesive strength levels necessary to keep the structure intact, which is less than 20 Pa, suggest a possibility of the asteroid's rubble pile structure, though this finding does not rule out its monolithic structure. These results can be validated with future James Webb Space Telescope observations. Our comprehensive characterisation can inform the planning of the Hayabusa2# rendezvous in 2031 and helps pave the way for future studies of dark comets.

Our understanding of kilometre-sized asteroids has advanced significantly thanks to in situ visits by space missions. The Hayabusa2 and OSIRIS-REx (Origins, Spectral Interpretation, Resource Identification, and Security-Regolith Explorer) spacecraft visited (162173) Ryugu[1] and (101955) Bennu[2], revealing two rubble-pile asteroids composed of thousands of boulders within the decametre range. Ryugu and Bennu are in the gravity-dominated regime; however, certain large boulders, such as Otohime Saxum at Ryugu's south pole, may exhibit characteristics more akin to the strength-dominated regime typical of decametre-sized asteroids.

Decametre-sized asteroids have been studied through remote observations, mainly from ground-based telescopes, and also via serendipitous detections in James Webb Space Telescope (JWST) mid-IR images reported in 2024[3]. Due to their smaller size and lower

A full list of affiliations appears at the end of the paper. ✉e-mail: tsantanaros@icc.ub.edu

brightness, these objects are difficult to observe, and their study is mainly limited to close encounters with Earth, which may occur only once every few years, depending on their orbits. 1998 KY_{26} will be the first decametre-sized asteroid ever visited by a spacecraft. The Japan Aerospace Exploration Agency (JAXA) Hayabusa2# extended mission will rendezvous with this asteroid in July 2031[4]. The mission aims to uncover the origin and formation of decametre-sized bodies, exploring potential connections to boulders observed on larger asteroids like Ryugu.

1998 KY_{26} was discovered on 1 June 1998 by the Spacewatch telescope at the Steward Observatory[5]. Despite its small size, the asteroid reached magnitude 16 thanks to its close approach to Earth, just 2 lunar distances away. Shortly after its discovery, optical and radar observations were made, as described by Ostro et al.[6], which remains the only publication to date providing a physical characterisation of 1998 KY_{26}. The spin period of 1998 KY_{26} was determined as 10.7 min, the fastest rotation period found by that date. This spin was used to fit the Doppler-based model, leading to an effective diameter for 1998 KY_{26} of (30 ± 10) m. By means of broad-band photometry, they also found the composition of the object to be analogous to carbonaceous chondritic meteorites.

1998 KY_{26} holds significant relevance for planetary defence, as its size is comparable to the Tunguska and Chelyabinsk impactors. Studying 1998 KY_{26} also contributes to establishing links between meteors and their parent bodies, as highlighted by impactor events such as 2023 CX_1 and 2024 BX_1[7,8]. Additionally, 1998 KY_{26} provides a valuable opportunity to bridge the understanding of size extremes within the near-Earth object (NEO) population, offering insights into the physical characteristics and behaviours of small asteroids. Its dimensions are also similar to the large surface boulders observed on asteroids (25143) Itokawa, (101955) Bennu, and (162173) Ryugu, making it a key target for studying the structural properties and composition of larger bodies.

Interestingly, 1998 KY_{26} has been observed to exhibit out-of-plane non-gravitational accelerations[9]. Some authors have attributed these forces to outgassing models, although no evidence of coma or dust tail has ever been observed, leading to the classification of 1998 KY_{26} as a member of the so-called inner dark comets[10].

Since 1998, the object has never been brighter than magnitude 24, preventing further physical studies, even with the largest telescopes. The first opportunity to resume studies of 1998 KY_{26} came in May-June 2024, when 1998 KY_{26} reached magnitude 20.2 during a close approach to Earth at 12 lunar distances. Studying the target of a space mission provides a unique opportunity to validate remote sensing techniques for small body characterisation.

In this study, we present the results of our observational campaign of 1998 KY_{26} during its 2024 close approach, providing a physical characterisation of the asteroid. Our findings indicate that 1998 KY_{26} has a smaller size, higher albedo, and shorter spin period than previously reported[6]. These results suggest the need to reassess the scientific objectives and mission operations of Hayabusa2#[4,11], while also highlighting the value of combining multiple remote sensing techniques for the study of decametre-scale objects.

Results

Our results are based on the combined optical observations from 1998, 2020, and 2024 and radar observations from 1998. 1998 KY_{26} was observed optically on 1998 June 2, 3, and 5 and with radar on 1998 June 6, 7, and 8[6]. Astrometric observations of the object were conducted with the VLT and Subaru telescopes on 2000 December 10. An additional dataset was obtained with the VLT telescope on December 12. The 2024 optical observations were collected over eight days, spanning from May 19 to November 7. Only the spring dataset achieved a sufficiently high signal-to-noise ratio (SNR) to generate lightcurves, whereas the fall dataset was used for phase curve analysis. On June 12, we obtained an additional dataset from SALT; however, due to its low SNR, it was used exclusively for astrometry (see Methods: Astrometry and Non-Gravitational Forces). The photometric observations were obtained under a variety of viewing geometries (see Supplementary Table 1 and Fig. 1), suggesting that the inferred spin period is half of the value originally published by Ostro et al.[6] (10.7015 ± 0.0004 min).

Our lightcurve inversion models to derive the spin and shape model indicate that the best fit corresponds to the period of (5.3516 ± 0.0001) min. Neither our Fourier analysis of the lightcurves nor the application of lightcurve inversion techniques revealed any evidence for a secondary periodicity indicative of a tumbling state. This strongly suggests that the object rotates about its principal axis.

In Fig. 1, we compare the lightcurve fits of the non-convex model presented in this paper (using a 5.35 min spin period) with the shape model from Ostro et al.[6] (using a 10.70 min spin period). The non-convex model fit yields an RMS of 0.106, while the Ostro et al. model results in an RMS of 0.162. Both models provide a good fit to the lightcurves observed at lower phase angles (as seen in the geometry of Ostro et al.), but only the non-convex model with a 5.35 min spin period accurately fits the lightcurves obtained at larger phase angles.

There is a reason why our result differs from Ostro et al. spin period. The 1998 optical observations were obtained under limited geometries, with the phase angle, the Sun-object-observer angle, ranging from 24° to 28°. Under this geometry, combining the observations with a 10.7 min period produced a lightcurve with sinusoidal pattern with two minima—consistent with the expected behaviour of a body rotating around its principal axis.

In contrast, our 2024 dataset spans phase angles from 5° to 101°. The lightcurve shapes changed dramatically over the apparition, with low-amplitude variations (about 0.3 mag) near opposition transitioning to large-amplitude variations (about 1.4 mag) at high phase angles. Observations at larger phase angles were crucial in resolving the ambiguity between the 5-min and 10-min spin solutions. While lightcurves gathered at phase angles of 20–30° yielded similar residuals for both periods, those obtained at larger phase angles strongly favoured the 5-min solution. This distinction arises from the more complex patterns in the lightcurves, driven by shadowing effects for non-convex shapes and angular characteristics for convex shapes (see Methods, Characteristics and Non-convex shape models).

The discovery of this shorter spin period has significant implications for the physical characterisation of 1998 KY_{26}. For example, the re-examination of the 1998 radar echo spectra using a first-order constraint based on measured bandwidths, a spherical shape assumption, and hard-wired rotation period of (5.35 ± 0.01) min, yields a smaller effective diameter for the object, as the diameter is proportional to the product of the bandwidth and spin period, bringing it down to (14 ± 2) m. We will refer to this as "shape-agnostic diameter". Thus, halving the spin period results in a reduction of the asteroid's size by a factor of two. Additionally, the radar albedo must quadruple (as it is inversely proportional to the geometric cross section).

Applying the Shaping Asteroid with Genetic Evolution (SAGE) modelling algorithm[12] and convex inversion methods[12,13] to the lightcurve observations, we derived shape models for 1998 KY_{26} (see Fig. 2). The preferred retrograde pole solution for SAGE was at the ecliptic longitude and latitude of $\lambda = 36°$ and $\beta = -44°$, in agreement with the preferred convex inversion solution at $\lambda = 29°$ and $\beta = -41°$. Typical mirror solutions for the pole orientation[14] were initially considered (see Methods, Characteristics and Non-convex shape models) but were rejected due to their poorer fit to both lightcurves and radar data. As an additional validation, we astrometrically measured our images and computed the orbit of 1998 KY_{26} using a non-gravitational acceleration model that combines radiation effects with outgassing-driven acceleration. Our analysis indicates that the preferred pole solution presented above is the sole model aligning within 1-σ of the poles derived

https://doi.org/10.1038/s41467-025-63697-4

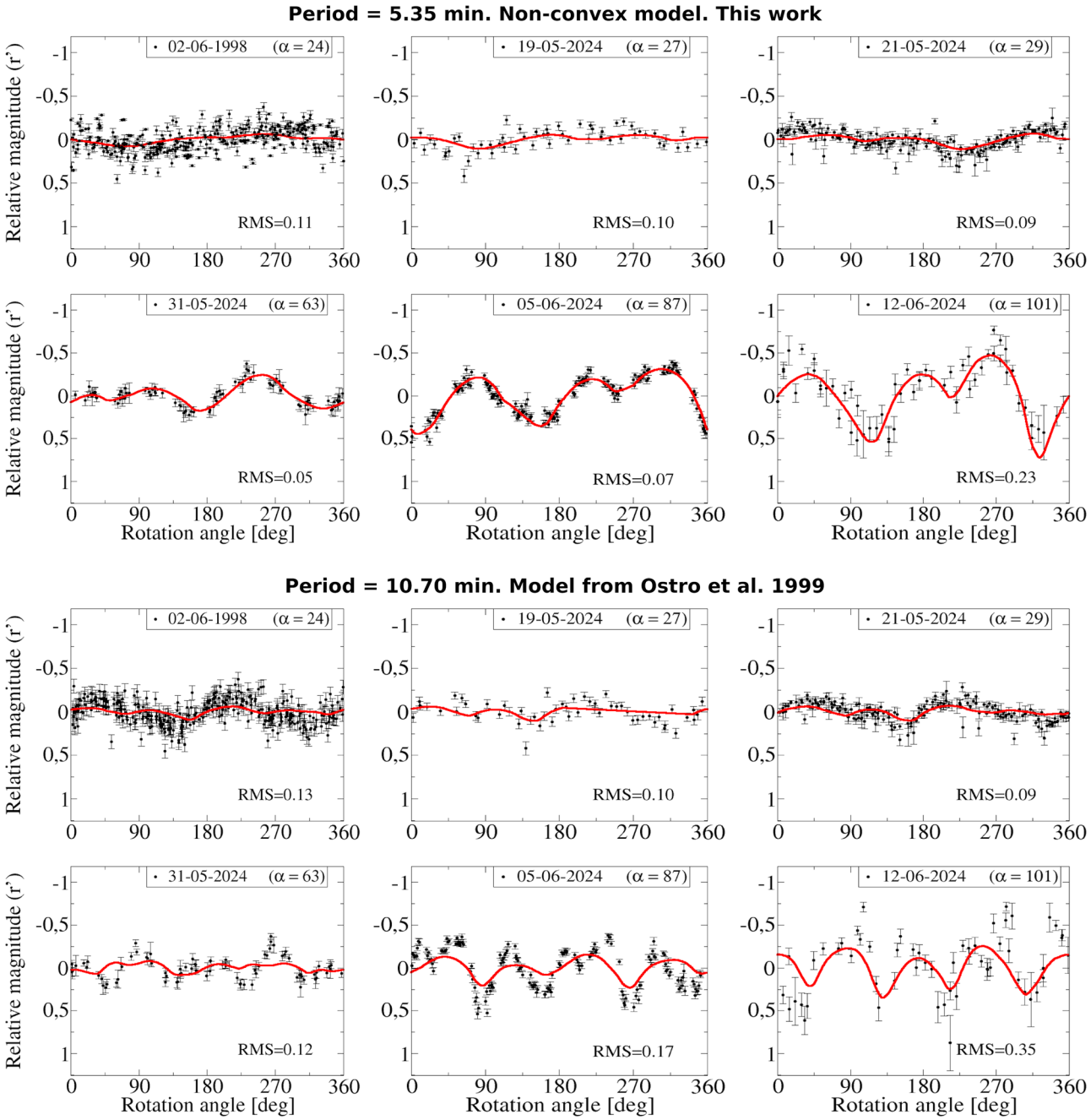

Fig. 1 | Comparison of lightcurve fits. The top panel shows the fit from the non-convex model presented in this paper, whereas the bottom panel compares it with the model from Ostro et al.[6]. The red line in each panel represents the synthetic lightcurve generated by the respective model. Black points represent the photometric lightcurves of 1998 KY_{26} for the 5.35 min and 10.70 min spin periods. Vertical error bars represent the photometric uncertainties derived from the measurement errors in each exposure. The solar phase angle, denoted by α, is indicated (in degrees).

from the orbital solution incorporating the non-gravitational model (see Methods, Astrometry and non-gravitational forces).

The preferred models were used to generate synthetic radar echo for comparison with the 1998 observations (see Fig. 3), allowing us to refine the diameter of 1998 KY_{26} to (11 ± 2) m – approximately one-third of the previously reported value in the literature[6]. This size corresponds to the specific spin-states and shapes produced with SAGE and convex inversion methods and is consistent within 3-σ with the "shape-agnostic" diameter of (14 ± 2) m.

The convex inversion method was used to constrain the absolute magnitude H and geometric albedo p_V for a fictitious spherical object with projected area equal to that of 1998 KY_{26} averaged over random orientation. From our 2024 absolute photometric observations, which covered phase angles between 5° and 101°, and treating the 1998 observations relatively, we derived H, G_1, G_2 models[15] for the phase curve (see Methods, Characteristics). Accounting for realistic opposition effect amplitudes, the absolute magnitude was estimated to be H = (26.13 ± 0.16) mag, which, for a nominal size of 11 m, yields a geometric albedo of p_V = (0.52 ± 0.08).

The geometric albedo of 1998 KY_{26} points to an Xe-type taxonomy: these are the only known asteroids with such high albedos. Further support for the classification comes from aubrites, enstatite achondrite meteorites[16]. Aubrites give rise to high albedos through their low-iron mineral composition predominated by enstatite and their brecciated structures including particles varying from μm scales to mm-scales in size, with substantial porosity due to the particulate

https://doi.org/10.1038/s41467-025-63697-4

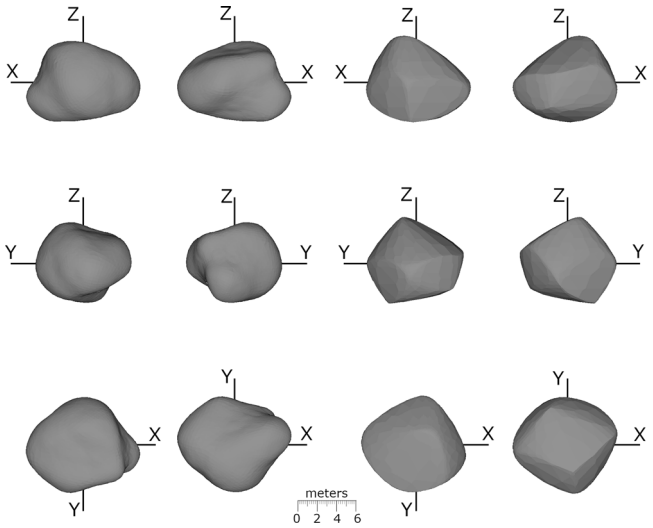

Fig. 2 | Shape models of 1998 KY$_{26}$. Non-convex shape model of 1998 KY$_{26}$ obtained with the SAGE inversion method (left) compared to the convex inversion solution (right). The model is shown from the perspective of each principal axis (X, Y, Z), which are defined as three mutually perpendicular directions forming a right-handed coordinate system. The rotation axis is aligned with the Z axis. Both SAGE and convex inversion shape models suggest that 1998 KY$_{26}$ is an asymmetric, moderately elongated object. The SAGE model shows a hint of a large concavity close to the southern hemisphere of the asteroid (negative Z-axis), which is interesting considering the small size of the object.

structures[17]. Such compositions and structures are known to result in narrow opposition effects[18]. An object with a regolith of small particles would produce a stronger opposition effect than a brecciated, monolithic object or an object with cm-sized or larger boulders.

On 30 May 2024, we obtained Sloan *griz* broadband photometry, revealing colours consistent with C-type and X-type asteroids (see Fig. 4). However, due to the high optical geometric albedo indicated by the phase curve analysis (see Methods), the most evident interpretation is that 1998 KY$_{26}$ is an enstatite-rich, Xe-type object of the X-group. Among all known asteroids, the Xe-types are the only group in the range of the high geometric albedos determined. This interpretation is also consistent with the asteroid's high radar circular-polarisation ratio of (0.5 ± 0.1)[6] based on statistical analysis of the polarisation ratios[19]. A plausible origin for this object is the Hungaria region, dominated by Xe-type class asteroids[20].

1998 KY$_{26}$ exhibits significant out-of-plane accelerations as found in previous studies[10] and confirmed by our astrometric measurements (see Methods, Astrometry and non-gravitational forces). One possible source of such non-gravitational acceleration is outgassing, as proposed by several authors[9,21]. To investigate the potential activity of 1998 KY$_{26}$, we analysed its profile in our frames by creating deep stack images. The 5-σ limits on the resolved dust mass around the object are below 0.5 kg, meaning that no dust particles have been detected around 1998 KY$_{26}$ at the epochs of our observations.

We also performed structural analysis using a finite element modelling (FEM) approach (see Methods, Structural Analysis) to quantify the asteroid's structural sensitivity at its fast rotation. Figure 5 displays the cross-sectional and surface distribution of the minimum cohesive strength, which is the lowest strength local elements should have to avoid structural failure. Because the asteroid's fast rotation causes tension-driven shear everywhere, all elements have positive minimum cohesive strength, meaning they should have structural sensitivity at some levels. A lower bulk density tends to have a lower minimum cohesive strength. However, as the bulk density increases, the minimum cohesive strength tends to be higher, particularly in the central region. A higher bulk density causes higher centrifugal and gravitational forces, resulting in higher structural loadings at local levels. When the bulk density is 4 g cm^{-3} (Fig. 5d, h), approximately equivalent to that for Xe-type asteroids, the central region reaches about 20 Pa, while the surface region generally reaches about 5 Pa, except for the southern surface. The central region having a higher minimum cohesive strength results from a combination of inward deformation along the spin axis and outward deformation on the equatorial plane[22,23]. A high minimum cohesive strength on the southern surface results from topographic depression, causing relatively large concavity.

It is not possible to gather new physical characterisation data for 1998 KY$_{26}$ from ground-based telescopes before the Hayabusa2# rendezvous in July 2031. The most promising (and likely the only) opportunity for obtaining new data is through the JWST. Observations by JWST-MIRI (the Mid-Infrared Instrument) could provide valuable constraints on the object's size, potentially further disproving the 30-m size estimate, and offering insights into its thermal properties. An attempt to detect 1998 KY$_{26}$ at mid-IR wavelengths[24] resulted in a constraining non-detection, which suggests a diameter smaller than 20 m. Based on our diameter estimate and shape modelling, we made long-term mid-IR flux predictions at various MIRI wavelengths. We identified two potential visibility windows between March 2028 and January 2029.

Discussion

This study highlights the potential of integrating various ground-based observational techniques to arrive at a detailed physical characterisation of small asteroids. The lightcurves we obtained enabled us to reject the previously published rotation period of 1998 KY$_{26}$ and to unambiguously determine its rotation period to be (5.35 ± 0.01) min. The lightcurves were acquired at different observing geometries, which allowed us to apply lightcurve inversion methods to obtain the object's spin-axis orientation and shape. In addition, using the newly derived rotation period and shape model, we re-analysed the 1998 radar data, which led to a revised, significantly smaller diameter estimate for 1998 KY$_{26}$ of (11 ± 2) m. This updated, smaller size is fully consistent with the non-detection by VISIR reported by Beniyama et al. 2025[24], providing independent validation of our findings. Finally, photometric measurements acquired over a range of phase angles enabled us to model the object's H, G_1, G_2 phase curve, yielding an updated absolute magnitude and placing constraints on its possible taxonomic classification. By combining the derived H value with the revised diameter from our radar analysis, we infer a high geometric albedo, consistent with an Xe-type asteroid.

However, our results also underscore the inherent limitations of remote observation methods. We note that asteroid size determination from radar data strongly depends on the period and pole solution. Particularly for small asteroids and low-SNR detections, where limited ranging information is available, it is crucial to collect the spin-state information through lightcurve observations to resolve this inherent degeneracy. Still, spacecraft visits show good agreement of radar size determination with ground-truth in-situ measurements[25,26].

The smaller size and higher albedo observed for 1998 KY$_{26}$ may also affect the calculations of the non-gravitational forces acting on it[9,27]. By incorporating the refined size, shape, and pole orientation, it would be possible to update the radiation models, potentially offering an explanation for the out-of-plane acceleration of 1998 KY$_{26}$. Additionally, the small size of the object suggests that processes like outgassing may not be viable. Moreover, our non-detection of dust particles around 1998 KY$_{26}$ also suggests that the object is inactive. Some studies[9,27] have classified 1998 KY$_{26}$ as a dark comet due to the anomalous out-of-plane accelerations observed in its orbit. However, the findings of this study remain at odds with the hypothesis of outgassing accelerations.

https://doi.org/10.1038/s41467-025-63697-4

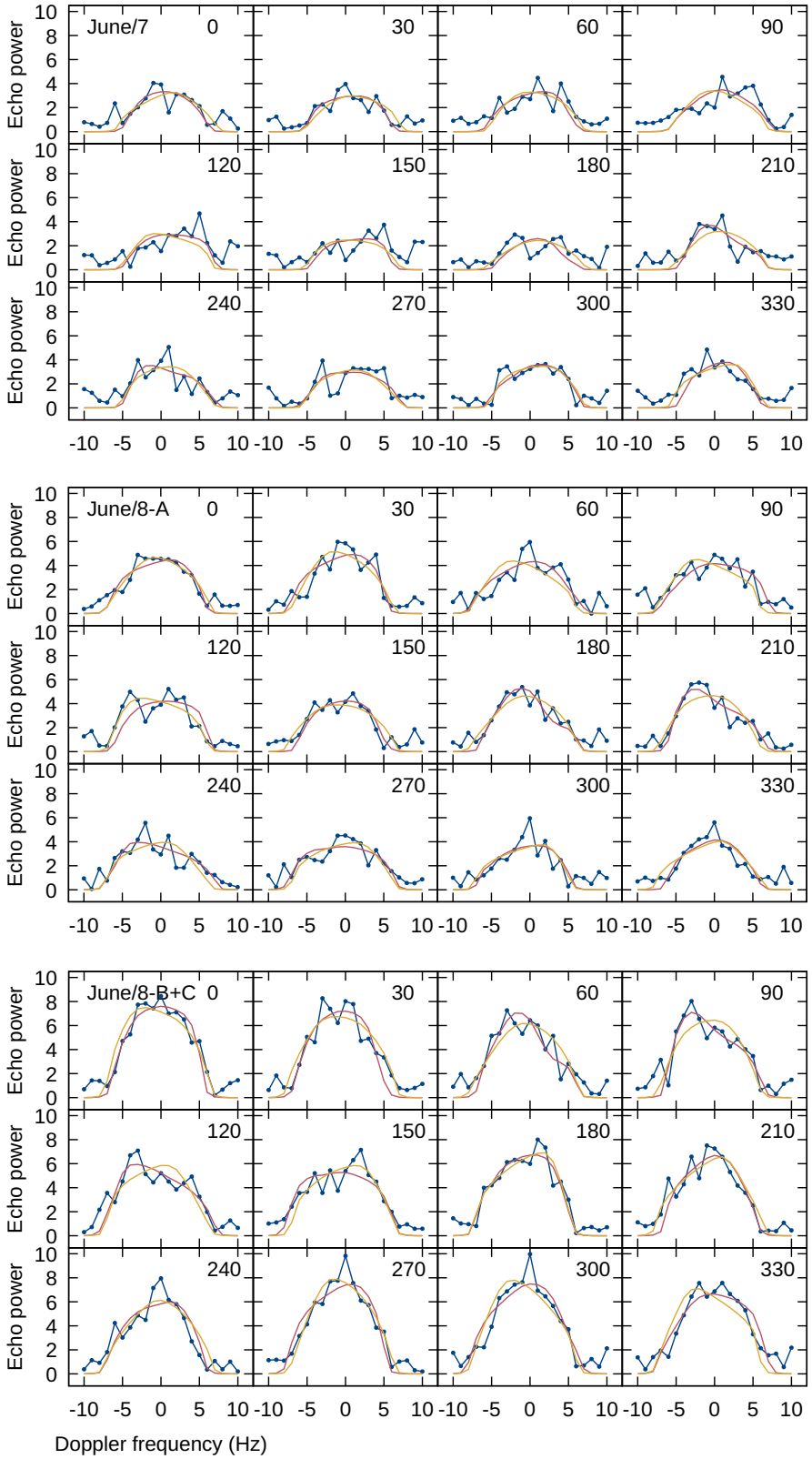

Fig. 3 | Model fits to radar data. Compilation of rebinned Doppler-only (continuous-wave) observations of 1998 KY_{26} collected on 7 and 8 June 1998 compared with synthetic echoes generated using models derived with lightcurve inversion methods. The radar data are marked with blue symbols, whereas the synthetic echo is drawn with a continuous red line for the best-fit non-convex SAGE model ($\lambda = 36°$, $\beta = -44°$) and the yellow curves represent the convex lightcurve inversion model ($\lambda = 29°$, $\beta = -41°$). The letters after the date are used to differentiate the datasets obtained on the same day. Datasets B and C obtained on 8 June were summed to increase the SNR.

https://doi.org/10.1038/s41467-025-63697-4

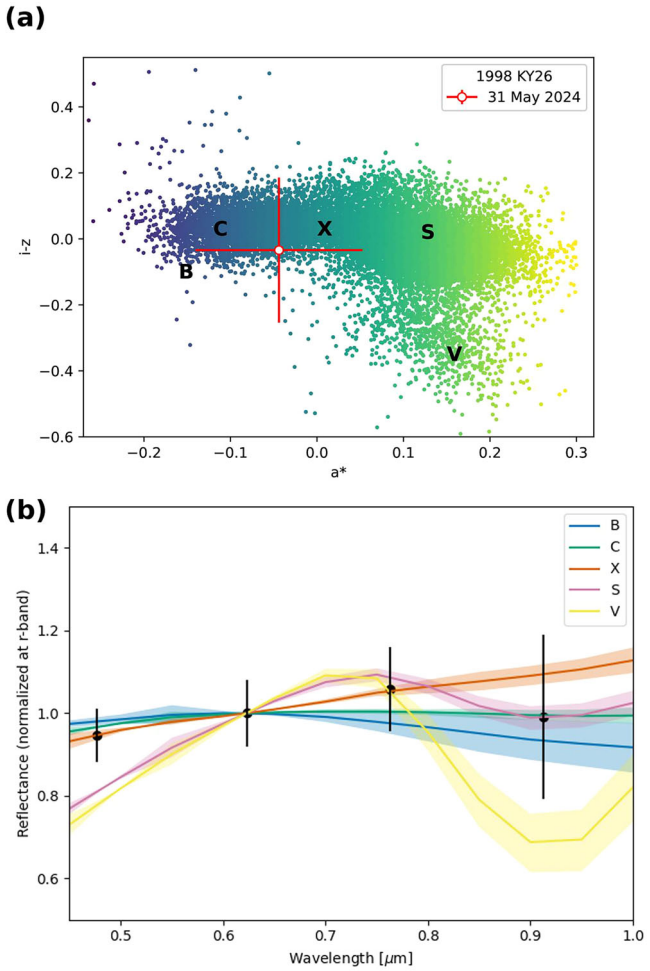

Fig. 4 | Taxonomic classification of 1998 KY_{26}. a The white dot shows our *griz* photometric measurement of 1998 KY_{26} from 31 May 2024, along with associated uncertainties. The background shows colour-coded points representing all asteroids of various taxonomic types from the SDSS MOC DR4 catalogue. Colour-coding corresponds to their position on the plot. The locations of the C, S and X taxonomic complexes, as well as the B and V type asteroids, are over-plotted for reference. Our measurement of 1998 KY_{26} is compatible with B, C, and X types. **b** The observed *griz* data (black points with 2σ error bars), normalized to the r-band (~ 0.62 μm), are compared with the major Bus-DeMeo taxonomic classes (B, C, X, S, and V). Shaded regions indicate the standard deviations of the corresponding templates, which have likewise been normalized to the r-band.

The derived minimum cohesive strength level of 1998 KY_{26} ranges between 4 and 20 Pa (Fig. 5), much smaller than the reported cohesive strengths of a few-hundred-metre diameter rubble pile objects, about 200–300 Pa[22,23,28,29]. This low cohesive strength level makes it possible for a rubble pile structure to exist at this body size and fast rotation. If this is the case, the asteroid's structure indicates the existence of high-level cohesion. If Van der Waals forces are a major contributor, the grain sizes may be as small as about μm[30,31]. Whether such grains are sufficiently available to glue larger boulders is an unresolved question, given the observations of Ryugu and Bennu that showed the lack of fine grains on their surfaces[30,31]. Also unresolved is the question of the formation –and survival against impacts– of such supposed small sand-piles, given their sub-cm-per-second escape velocities[32]. While the rubble pile scenario stands as stated, given the asteroid's formation processes, a monolithic structure may still be sound. Tens-of-metre diameter monolithic fragments can be generated easily by catastrophic disruption[33] or by fission of a larger body by spin-up processes. As a matter of fact, a rubble pile structure needs a re-aggregation process of fragments. A high angular momentum creating a Roche Lobe smaller than the asteroid's size may prevent the re-aggregation process, leading to the formation of a fast-spinning rubble pile object. However, non-gravitational torques driven by impacts[34,35], outgassing[10], and thermal radiation[36] may accelerate the asteroid's spin state after the rubble pile structure formation, though this scenario still lacks feasibility due to uncertainties of many possible factors. In a hybrid scenario, the asteroid might be a large single boulder, but its surface may be covered by fine grains around the poles, where spin acceleration is minimal.

Planetary defence is a global initiative aimed at preventing asteroid-related hazards and assessing their risks. Decametre-sized asteroids are the most common objects that could cause critical effects on human activities if they impact the Earth[37]. Among the significant properties of hazardous objects in this effort are orbit, mass, and strength[38]. The present comprehensive observational campaign demonstrated the capabilities of Earth-based observations of measuring the physical properties of decametre-sized asteroids, which is a key demonstration of planetary defence. Furthermore, such measurements also enabled structural constraints on a target's strength. Therefore, Hayabusa2#'s detailed study of a decametre asteroid will significantly enhance our understanding of the physical characteristics of the most frequent Earth-impacting objects. Additionally, gaining insights into the non-gravitational forces acting on these bodies will enable more accurate orbit predictions. This knowledge is critical for future planetary defence operations, where it will help identify and mitigate potential impact threats.

The Hayabusa2# spacecraft is scheduled to visit 1998 KY_{26} in 2031, providing an opportunity to validate our multi-technique, remote characterization methods for decametre asteroids. This is an important element in the context of discoveries of potential hazardous asteroids in the future. However, 1998 KY_{26}'s smaller size, faster rotation, and higher albedo present challenges for mission operations. For instance, plans to fire a tantalum projectile to create a crater may need to be reconsidered due to the asteroid's size. Additionally, its rapid rotation could complicate operations for instruments requiring longer integration times. On the positive side, the absence of detectable dust around the object could facilitate close-proximity operations. Importantly, these factors have been identified six years ahead of the rendezvous. If successful, Hayabusa2# will provide invaluable in situ data on a rare bright decametre object, offering unique insights into this class of asteroids.

Methods

Photometric observations

We obtained optical photometry of 1998 KY_{26} during May-June and October-November apparitions in 2024. Observations were made on eight different nights, yielding five lightcurves under varying observing geometries (see Fig. 1).

Due to the faint magnitude of the object during these apparitions (ranging from 20.3 mag at its brightest to 23.9 mag at its faintest), we utilized four large-aperture telescopes: the Gran Telescopio CANARIAS (GTC) with the Optical, Spectroscopic, and Infrared Remote Imaging System (OSIRIS) instrument, the Very Large Telescope (VLT) with FOcal Reducer and low dispersion Spectrograph 2 (FORS2), Gemini South with the Gemini Multi-Object Spectrograph (GMOS), and the Víctor M. Blanco Telescope with the Dark Energy Camera (DECam). All observations were conducted using r' broad-band Sloan filters, except for the VLT/FORS2 observations, which employed the $R_{SPECIAL}$ band. Additionally, we obtained five *griz* cycles with Sloan filters to study the object's taxonomy.

Exposure times were determined based on the object's apparent motion and the seeing conditions at each site. To ensure accurate measurements, we adjusted exposure times so that the object and

https://doi.org/10.1038/s41467-025-63697-4

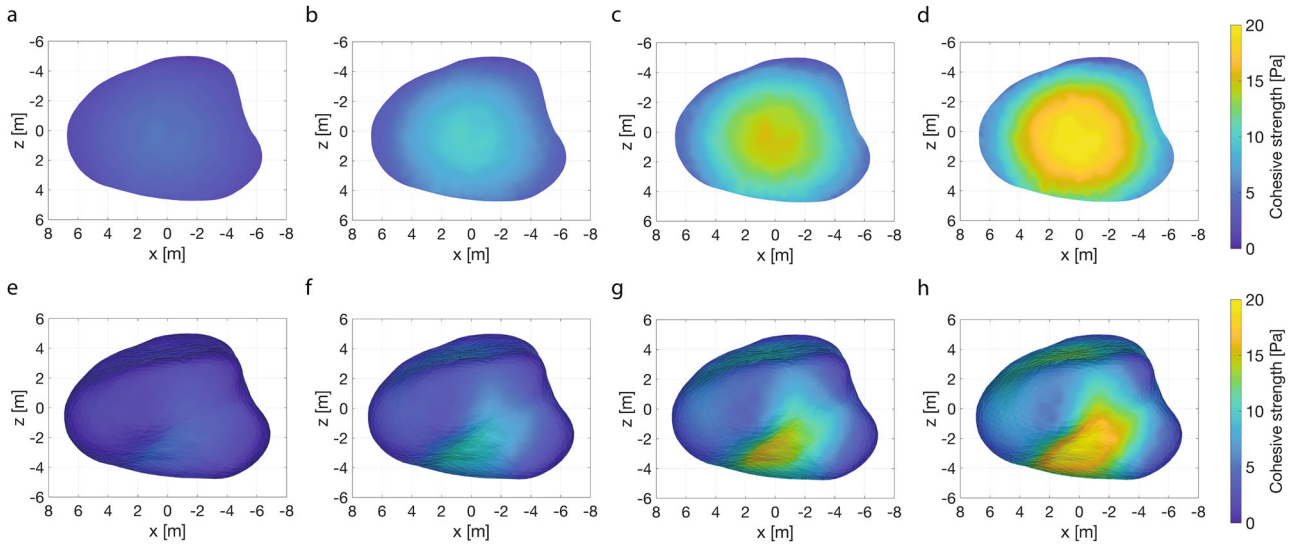

Fig. 5 | Interior structure of 1998 KY_{26}. a–d Crosssectional distribution of the cohesion in the x–z plane; **e–h** surface distribution over the same plane. Minimum cohesive strength distribution in Pa for the asteroid's interior and at the surface. We considered four bulk density cases (ρ = 1-4 g cm^{-3}) and we assumed principal axis rotation with the spin axis fixed along the z axis. A higher minimum cohesive strength implies that a greater structural integrity is required to maintain the stability of local elements.

stars remained point-sources, limiting their motions to no more than 1.5 times the seeing during each exposure.

Photometric reduction of each dataset was performed using standard procedures, including bias correction and flat-fielding, to produce the lightcurves shown in Fig. 1. Non-variable solar analogue stars were selected as reference targets in each field, ensuring that their brightness was similar to that of 1998 KY_{26} (with a difference of no more than 1.5 magnitudes). The OSIRIS data was processed with the SAUSERO pipeline[39] for bias, flat-fielding. Gemini GMOS data was acquired through the Gemini Observatory Archive[40] at NSF NOIRLab and processed using DRAGONS (Data Reduction for Astronomy from Gemini Observatory North and South)[41,42]. The DECam basic reduction was performed using the DECam Community Pipeline[43] for bias, flat-fielding, illumination correction, and astrometry.

A summary of the observation dates, strategies, conditions, and telescopes used is provided in Supplementary Table 1, which also includes observations from the discovery apparition.

Characteristics

In Fig. 4, panel a, we present the $i - z$ and a^* colours of 1998 KY_{26} in comparison to the colours of asteroids observed during the Sloan Digital Sky Survey (4th data release). The a^* colour was estimated from $a^* = 0.89(g - r) + 0.45(r - i) - 0.57$[44]. From the Sloan Digital Sky Survey (SDSS) catalogue, we selected only those objects which fulfil the quality criteria as found in the literature[45]. The locations of the taxonomic C-, X-, and S-complexes as well as the B- and V-type asteroids are indicated. The colours of 1998 KY_{26} are consistent with those of objects in the complexes B, C and X.

In Fig. 4b, we compare our *griz* measurements with the spectral templates of the major asteroid taxonomic classes, showing that our data are compatible within 2σ with the B, C, and X taxonomic classes, but deviate from the S and V class due to discrepancies at 0.47 μm.

The rotation period, pole orientation, shape, and surface scattering properties were constrained using convex inversion methods[13,46–48] for the complete photometric dataset spanning more than 26 years from 1998 to 2024 (see Supplementary Table 1). The specific inversion method by Muinonen et al.[13,48] supports an absolute treatment of the photometric observations and allows for the derivation of the absolute magnitude H for a spherical object with a projected area equal to that of 1998 KY_{26} averaged over random orientation.

First, using relative treatment of the 11 lightcurves, the rotation period was systematically scanned for a small number of pole orientations, with roughly 30° resolution on the unit sphere, by optimizing both the shape and the pole orientation for each trial period. Rotation periods in the proximity of $P = 0.089193h$ (5.352 min) were confirmed to yield superior fits to the photometric data, ruling out the earlier period of roughly double the value[6]. Within the time span of the observations of T_{arc} = 9655.25 d, an extreme time resolution of 36 μs ($< P^2/2T_{arc}$) was utilized in the systematic scans, securing an unambiguous analysis in terms of the number of rotations. Four candidate pole orientations were identified (see Table 1). The periods and pole orientations were further refined in the vicinity of the initial values.

Second, moving to absolute treatment of the lightcurves (except for the continued relative treatment of the ones from 1998), the four pole orientations and shapes were further optimized together with the H, G_{12} phase function[15], keeping the rotation periods fixed. It became clear in all four cases that the G_{12} parameter had to correspond to values typical for asteroids with high geometric albedos. The general H, G_1, G_2 phase function[15] was then incorporated for a systematic mapping of scattering solutions within the G_1, G_2 plane. Due to the lack of photometric data within phase angles $< 5°$, the values of the parameters were varied from the domain of a substantial opposition effect amplitude typical for large Xe-type asteroids such as (44) Nysa to the domain of a negligible opposition effect. In detail, the G_1, G_2 parameters were varied linearly from (G_1, G_2) = (−0.2, 0.9) through (−0.15, 1.0) to (−0.1, 1.1). It was confirmed that the shapes and pole orientations were insensitive to the assumed G_1, G_2 parameters. The four reference solutions with realistic parameter values of $G_1 = -0.15$ and $G_2 = 1.0$ are listed in Table 1.

Table 1 provides two types of uncertainties for the pole orientations from the convex model. The systematic scans for the rotation periods were repeated, using absolute convex inversion with $G_1 = -0.15$ and $G_2 = 1.0$, for the period intervals and time resolution used in relative convex inversion. Consequently, the rotation periods changed, typically in multiples of roughly 124 μs, within the scan intervals utilized. In Table 1, the approximate full scan intervals are described by the uncertainties expressed next to the rotation periods, whereas half the scanning step is given in parentheses, thus describing the

Table 1 | Best spin and pole solutions of 1998 KY_{26} obtained with the convex and SAGE modelling techniques, ordered by goodness of fit

Solution	λ (°)	β (°)	Spin period (min)	rms-value
Convex#1	29 ± 7 (± 1)	− 41 ± 7 (± 2)	5.3515986 ± 0.00018 (± 0.0000003)	0.106
Convex#2	208 ± 14 (± 1)	37 ± 7 (± 2)	5.3512902 ± 0.00036 (± 0.0000003)	0.108
Convex#3	225 ± 3 (± 1)	− 38 ± 6 (± 2)	5.3516346 ± 0.00018 (± 0.0000003)	0.113
Convex#4	287 ± 13 (± 1)	31 ± 20 (± 1)	5.3513970 ± 0.00012 (± 0.0000003)	0.117
SAGE#1	36^{+6}_{-5}	-44^{+12}_{-10}	5.3516 ± 0.0001	0.106
SAGE#2	232^{+6}_{-7}	-44^{+22}_{-9}	$5.3516^{+0.0028}_{-0.0002}$	0.107
SAGE#3	47^{+8}_{-4}	37^{+14}_{-17}	$5.3513^{+0.0001}_{-0.0002}$	0.111
SAGE#4	262^{+13}_{-12}	61^{+26}_{-17}	$5.3513^{+0.0028}_{-0.0058}$	0.114

The convex solutions include two uncertainties: the ones next to the parameter values refer to the full range of plausible periods and the ones in parentheses refer to Markov chain Monte Carlo (MCMC) 1-σ values for a period fixed to the best solution given. The latter uncertainty for the period refers to the approximate interval between plausible discrete periods allowed by the photometric data.

maximum uncertainty of the period. For the pole orientations, the uncertainties next to the longitudes and latitudes have been computed using the χ^2-values from the systematic scans. Thus, they refer to the full inversion across plausible periods. In parentheses, Markov chain Monte Carlo (MCMC) uncertainties are given, keeping the periods fixed in the absolute MCMC convex inversion for shapes, pole orientations, and G_1, G_2 parameters. It is clear that, for such discrete values of the period, the pole orientations become tightly constrained.

For the nominal diameter of D = 11 m, the absolute magnitude H = 26.13 mag of our reference pole solution Convex 1 would give a geometric albedo of p_V = 0.5155. A Nysa-like opposition effect would give H = 25.97 mag and p_V = 0.5974, and the limit of no opposition effect would give H = 26.27 mag and p_V = 0.4532. To conclude, we arrive at H = (26.13 ± 0.16) mag and p_V = (0.52 ± 0.08), results that are insensitive to the solutions for the rotation period, pole orientation, and shape.

The originally reported opposite-circularly (OC) polarized radar-albedo range of 0.012–0.11 was derived from a radar cross section of (25 ± 10) m^2 and the estimated diameter range of 20–40 m. Using the diameter estimate of (11 ± 2) m, the corresponding range of the OC radar albedos is 0.11–0.55, with 0.26 as the average from the radar cross section of 25 m^2 and a diameter of 11 m. Considering the whole near-Earth asteroid (NEA) population, OC radar albedos greater than 0.4 are rare and only observed for metal-rich objects, whereas values below 0.1 are mostly observed for C-type objects[49]. The derived range covers a majority of NEAs in the S and X complexes, and is too wide a range for useful constraints.

The radar circular-polarisation ratio of (0.5 ± 0.1) is unusually high, with 95% of the NEA population below this range[19]. Regardless, only few definitive constraints can be made. Based on the statistical analysis of the polarisation ratios of NEAs[19], C-, S-, and Q-type asteroids have typically polarisation ratios up to 0.6, whereas V types have polarisation ratios 0.4–1.0. The range has been shown to depend on the abundance of wavelength-scale regolith particles on or near the object's surface, so that a greater abundance of wavelength-scale (centimetre-scale in X-band observations) particles increases the polarisation ratio[50]. For the X complex, polarisation values up to 1.4 have been measured[19]; however, specifically Xe-type is typically consistent only with polarisation ratios of 0.5 or greater. Thus, while the polarisation ratio of 1998 KY_{26} is relatively high and as such consistent with the Xe-type classification, it does not fully rule out other taxonomic types, unless we assume that due to the rapid rotation, there is a deficit of centimetre-scale or smaller particles. A statistically confident identification of an Xe-type asteroid based on the polarisation ratio would require a value greater than 0.82[19].

Non-convex shape models

In addition to the convex solutions obtained during the phase curve fit, we explored non-convex shape solutions of 1998 KY_{26} using the genetic algorithm SAGE[12]. This technique is capable of determining non-convex shapes, spin axis orientations, and rotational periods for asteroids, provided their lightcurves offer sufficient geometric coverage and photometric quality. The asteroid's shape is represented as a 3D mesh consisting of vertices and triangular faces. These vertices are distributed along fixed rays emanating from the centre of the asteroid. The process starts with a simple shape (e.g., a sphere) and a randomly oriented rotation axis. In each iteration, new asteroid models are generated by introducing random variations to the shape and orientation. These variations are similar to genetic mutations, with each new generation inheriting the parameters of the best-fit previous models. Synthetic lightcurves are generated for each model using a computationally intensive process that accounts for the asteroid's orientation, rotation, and illumination conditions. These synthetic lightcurves are then compared to the observed data using a root mean square deviation (RMS) metric. The model with the lowest RMS (i.e., the best match to the observed lightcurve) is selected as the basis for the next generation. Lightcurves are computed using a combined scattering model (Lambert and Lommel-Seeliger laws) to simulate how the asteroid's surface scatters light. Shadows from concave features are also accounted for, which adds computational complexity. The rotation period is a critical parameter and is refined during each iteration. A grid search is performed to identify the period that minimizes discrepancies between observed and synthetic lightcurves. The algorithm ensures convergence by adjusting the weights assigned to different lightcurves, focusing on poorly reproduced observations in subsequent iterations to avoid local minima. The final model is chosen when the RMS stabilizes, indicating that the genetic algorithm has converged to a solution that best fits the observed data. This process can produce multiple models if the data is insufficient to resolve ambiguities, such as prograde vs. retrograde rotation[14]. Each modelling run produces a family of solutions—variations of the model that fit the observed data. When sufficient observational data is available, these models converge to a single, well-defined shape.

We derived four distinct shape and spin solutions –two retrograde and two prograde– consistent with those obtained using the convex model. These solutions are not completely independent; instead, they are a characteristic of the inverse problem, which yields mirrored solutions of the shape and spin vector[51]. The best-fitting shape model, corresponding to pole solution #1 in Table 1, is shown in Fig. 2. This solution also gives the best fit to radar data and to the non-gravitational model. All four solutions suggest a roughly spherical object, with the best solution #1 displaying a prominent concavity near the south pole. Shape uncertainties were estimated following the methodology outlined in ref.[52] and are shown in Supplementary Fig. 1 for the best found solution #1. The uncertainties are latitude-dependent: approximately 15% at the equator and 40% near the poles. The greater uncertainty near the poles arises from the comparatively

https://doi.org/10.1038/s41467-025-63697-4

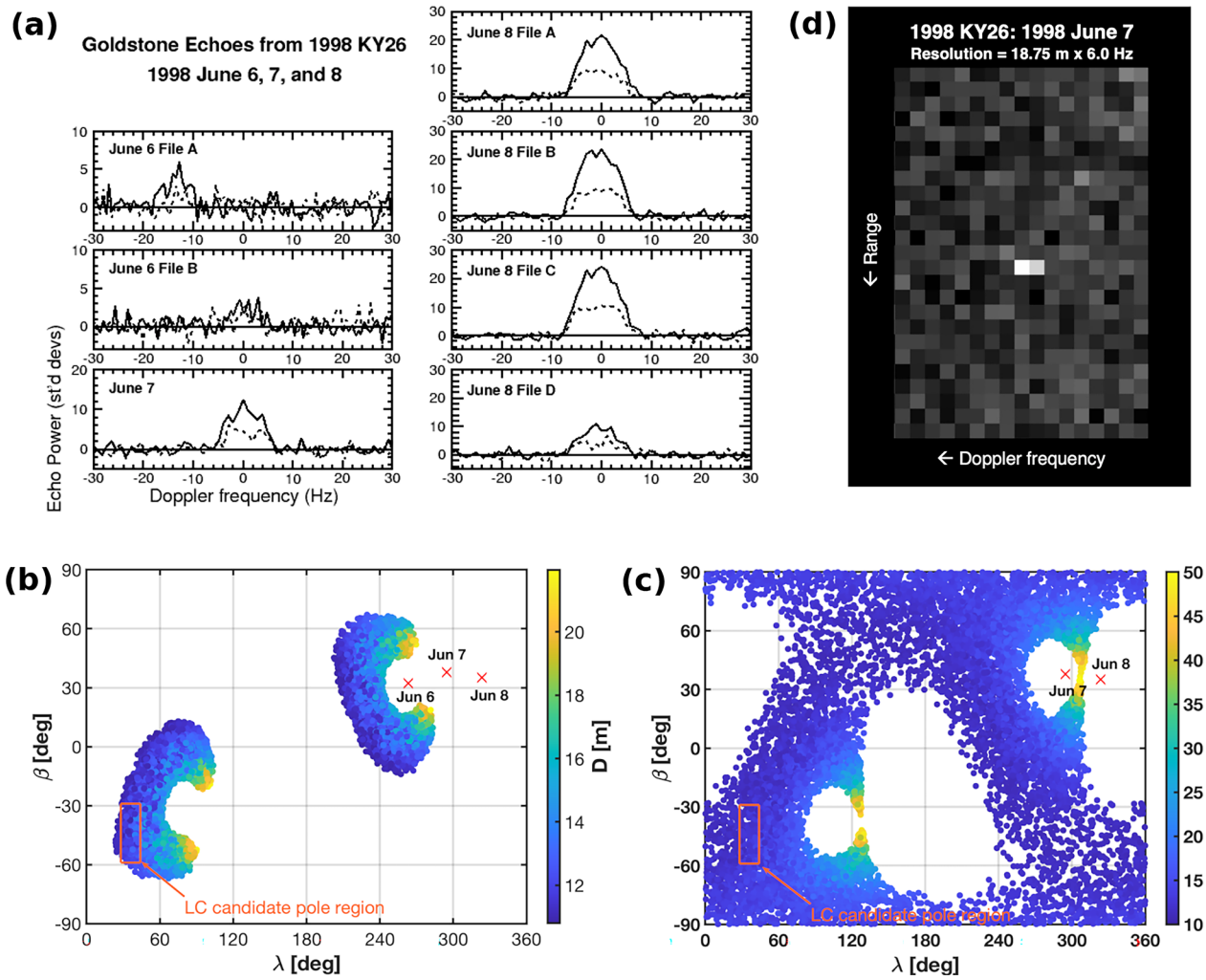

Fig. 6 | Spin and size from radar data. a Goldstone echo power spectra of 1998 KY_{26}. Collage of echo power spectra obtained on 1998 June 6, 7, and 8. Each panel shows a weighted sum of all the data from individual data taking intervals. When more than one set was created for a given date, the sets are labelled A, B, C and D. **b** Ecliptic longitude and latitude of 10 000 candidate poles constrained by three days of radar data (see Supplementary Table 2). The colour scale represents the diameter distribution. The red markers show observer-centred ecliptic longitude and latitude of the target centres' apparent position. The orange box marks the pole region constrained by the lightcurves. **c** spin pole constraints based on two days of radar data. **d** delay-Doppler image obtained on 1998 June 7. The image has dimensions 468.75 m x 68 Hz and the resolution is 18.75 m x 6 Hz. Time delay (range) increases down and Doppler frequency increases to the left. The asteroid echo is contained within a single range bin, 18.75 m.

superior photometric coverage of the equatorial regions, which benefits from more favourable observing geometries.

Comparing the non-convex and convex solutions, there are differences in the RMS-values obtained for the three mutually agreeing pole solutions (see Table 1). However, the differences are small, and they can derive from a number of methodological differences. First, the models for the observational uncertainties differ for SAGE and the convex inversion method. Second, the present convex inversion method makes use of a pure Lommel-Seeliger surface scattering model, whereas SAGE utilizes a combined Lommel-Seeliger and Lambert model. Third, the SAGE rms-values refer to a relative treatment of the lightcurves, whereas the rms-values from convex inversion refer to an absolute treatment of the lightcurves. In summary, the differences are inconsequential insofar as the results of the present work are concerned.

Reprocessing of the 1998 radar data

With the period established, we decided to re-examine the radar observations collected on June 6-8, 1998 with Goldstone (see Fig. 6 and Supplementary Table 2). The asteroid traversed 49.5° across the sky during this time. We first used just the bandwidth measurements to find constraints on pole direction and size. The Doppler broadening of the echo is a function of the asteroid's rotation period, diameter, and spin axis orientation with respect to the radar line-of-sight[53]:

$$B = \frac{4\pi D}{\lambda P}\cos(\delta) \quad (1)$$

where B is the bandwidth, D is the object's maximum breadth in the plane of the sky perpendicular to the spin vector, λ is the radar wavelength, P is the rotation period, and δ is the sub-radar latitude. The averaged bandwidth doubled between June 6 and 8 suggesting that the radar line-of-sight moved closer to the equator.

We did a Monte Carlo type of fit to the bandwidths observed on June 6-8, Supplementary Table 2, based on Eq. (1). Figure 6 shows rotationally unresolved spectra, based on the data sum obtained during the same observing interval. As such, they represent maximum observed bandwidths and the largest physical extents of the object recorded on each day. We uniformly sampled 10,000 times three bandwidths that are within the ranges reported in Supplementary

Table 2. Our goal was to find the pole directions and sizes that reproduce these synthetic measurements. The period was held fixed within (5.35 ± 0.01) min. We assumed that the object's diameter is 8-50 m and there were no constraints on the pole direction. The plot shows 10,000 candidate solutions. The mean diameter measured this way was (14 ± 2) m (1-σ) and the maximum diameter was 22 m. The radar data allow both prograde and retrograde pole solutions, and the retrograde pole region overlaps with the candidate pole region determined by the lightcurves (Fig. 6). This pole region clearly prefers smaller diameter for 1998 KY_{26}, $D < 15$ m.

The shape model and size estimates published back in 1999[6] were based on the assumption of rotation period that was a factor of two shorter that the current estimate. The modelling only included the continuous-wave (cw) spectra from June 7 and 8, 1998 because the SNRs were sufficiently strong on these days, and the rotation of the object was resolved. For the analysis we describe in this section, we do not use the rotationally resolved spectra, but long interval sums. This allows us to include the data from June 6, (Fig. 6). These data had lower SNRs, but the echo is clearly visible, and we found that it significantly helps constrain the pole direction as well as the object's size, as seen by comparing the panels in Fig. 6. We note that both the current and past size estimates are consistent with the diameter being < 40 m, the upper limit established from the ranging imaging, where the asteroid fits in a single ranging row (Fig. 6).

We then further refined the size estimation by combining the subset of cw observations previously used in shape modelling of 1998 KY_{26}[6] with the outcomes of both SAGE and convex lightcurve inversion. The observations are grouped into three sets, one collected on 7 June 1998 (see Fig. 6) and the other two on 8 June 1998. The original period determination reported was double the period reported here. The data collected during bistatic observations, where DSS-14 was continuously transmitting and DSS-13 was continuously receiving, contained many rotations of the object. The signal was processed so that the data that contain the same 15° of rotation were summed together to increase the SNRs. This yielded 24 snippets of raw data covering the 360° of rotation. Each portion of the raw data was Fourier transformed into an echo power spectrum. Having established that the rotational period is actually 5.3516 min, we have summed pairs of spectra corresponding to the same rotational phase ranges to obtain 12 cw spectra for each of the three observations, each now corresponding to 30° of rotation. We then run a simple fit with established radar modelling methods[54,55], fitting the overall size of the object, but using the best-fit spin-states and shapes produced using SAGE and convex inversion. Both optical-lightcurve-inversion models produce good fits to the radar data for a diameter of (11 ± 2) m, which, given the uncertainties, is consistent with the size estimate based on radar echo bandwidths alone. What is more, the model spectra for the non-convex model reproduce the asymmetry noticeable in observations, particularly in data collected on June 8 (Fig. 6).

Internal structure

We apply an in-house finite element modelling (FEM) approach[56] developed by one of the authors to quantify the internal structure of 1998 KY_{26}. The applied FEM has been validated for the last decade with detailed comparisons with theoretical modelling and discrete element modeling (DEM), demonstrating its consistency and thus becoming one of the standard approaches in small body structural analysis[57–60]. Both models are widely used to characterize geologic targets of various sizes. Our focus is to roughly calculate the stress field and thus a lower bound of the mechanical strength of 1998 KY_{26} without adding free parameters. FEM, similar to DEM, can compute a stress field consistent with theoretical prediction[59–61]. Our approach applies a linear elastic model, assuming that elasticity solely holds the stress field. We assume Young's modulus and Poisson's ratio to be 10^7 Pa and 0.25, respectively. The boundary condition constrains the translational and rotational modes at the central point[56]. Based on our spin pole measurements, the model considers the asteroid's static condition by considering that its rotation is in the principal axis mode along the smallest moment of inertia axis at a spin period of 5.35 min, equivalent to 0.0196 s^{-1}. We develop an FEM mesh model for this study by performing the following steps. First, we shrink the size of the observation-driven polyhedron non-convex shape model. We use MeshLab[62] to employ Quadric Edge Collapse Decimation to reduce the shape size to 1922 vertices and 3840 faces. Then, we apply the tetgen code[63] and the derived shape model to develop a four-node mesh model with 5347 nodes and 26,796 elements. Finally, the resulting FEM model, however, has a volume of 1.59 m^3, equivalent to an equivalent diameter of 3.12 m. This smaller size results from the original shape model's scale. We factor all the node positions by 3.53 to achieve the 11 m equivalent diameter.

The current model quantifies the internal stress condition by computing how sensitive structural elements are to failure. One way to characterise this condition is to determine the strength to keep a local element structurally intact. The minimum cohesive strength is the minimum mechanical strength for a local element to be away from structural failure. The condition is computed using the Drucker-Prager yield criterion with perfect plasticity[64]:

$$Y = \frac{\alpha I_1 + \sqrt{J_2}}{\beta}, \tag{2}$$

where

$$\alpha = \frac{2\sin\psi}{\sqrt{3}(3-\sin\psi)}, \tag{3}$$

$$\beta = \frac{6\cos\psi}{\sqrt{3}(3-\sin\psi)}. \tag{4}$$

In Equation (2), I_1 and J_2 are the stress invariants, and ψ is the friction angle. Throughout the analysis, we fix ψ at 35°. If the minimum cohesive strength level is zero, local elements do not need any strength to keep them structurally intact. A high minimum cohesive strength indicates the sensitivity of local elements to structural failure. We compute the minimum cohesive strength at all the defined nodes to visualize its distribution.

We consider a bulk density range between 1 and 4 g cm^{-3} to visualize how a different bulk density controls the internal structure. Our photometric measurements prefer that this asteroid is classified as Xe-type, though its colours are consistent with C-complex and/or X-type. Thus, the defined bulk density range accounts for these types. Xe-type asteroids are, in general, reported to be rich in enstatite. The bulk density for this material is between 3.15 and 4.10 g cm^{-3} [65]. C-complex asteroids have bulk densities as low as 1 g cm^{-3}, based on detailed observations of asteroid (162173) Ryugu by Hayabusa2[1]. X-type asteroids with higher albedos, usually classified as Xe-type, exhibits a weak 0.9 μm absorption and a deep 0.5 μm absorption[66]. This feature infers a possible link to enstatite achondrite[16,67], which may originate from the Hungaria region at high inclination[16,68]. We simulate four bulk density cases with the defined range at an interval of 1 g cm^{-3} (Fig. 5).

Testing the 1998 KY_{26} results via JWST observations

The Hayabusa2# mission will rendezvous with 1998 KY_{26} in July 2031: the first visit of a fast-rotating decametre-sized asteroid. In the time period between 2025 and the arrival in 2031, 1998 KY_{26} will be very challenging to observe from Earth (always fainter than V-magnitude of 24.7). However, JWST, with its sensitive mid-infrared imager MIRI, will be able to detect it[33,69] and to test some of the properties we derived from lightcurves and radar measurements. The conducted JWST MIRI

https://doi.org/10.1038/s41467-025-63697-4

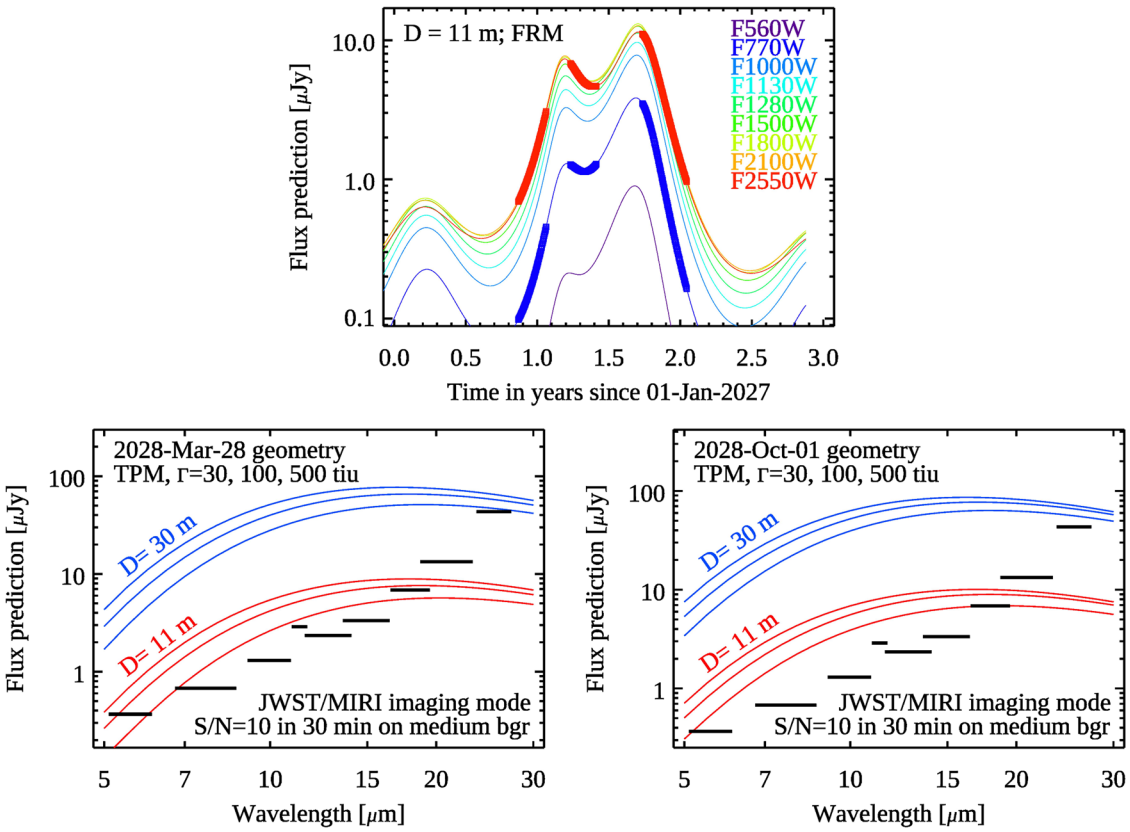

Fig. 7 | James Webb Space Telescope (JWST) visibility windows to observe 1998 KY_{26}. Flux predictions (in μJy) for 1998 KY_{26} for possible future JWST-MIRI (JWST's mid-infrared imager) observations. Top: Fast rotating model (FRM) fluxes for the specific MIRI bands for the years 2027 to 2029, JWST visibility windows are indicated by the thick blue and red lines. Bottom: Thermophysical model (TPM) flux predictions for two different sizes, 30 m and 11 m, assuming the SAGE#1 spin properties, for a wide range of thermal inertias, and for two epochs (left: 2028-Mar-28, right: 2028-Oct-01). The MIRI S/N = 10 sensitivity limits for 30 min integration per filter (assuming a medium sky background) are shown as solid black lines. JWST-MIRI measurements would allow to settle the size question and to constrain the object's thermal properties well before the Hayabusa2# arrival in 2031.

measurements of the potentially hazardous asteroid 2024 YR_4[70] demonstrated that moving targets at the 1–10 microJy level, as expected for 1998 KY_{26} with a diameter of 11 metres during upcoming JWST visibility windows, can be detected with SNRs >> 25 within 20 min exposure time in the F1000W, F1280W, and F1500W bands. The upcoming JWST visibility windows (solar elongations between 85° and 135°, as seen from JWST close to the Lagrangian point L2) are listed in Supplementary Table 3.

We made long-term mid-IR flux predictions at different MIRI wavelengths by using the fast-rotating model (FRM, [ref.[71], and references therein]), see Fig. 7 (left side), and more sophisticated thermophysical model (TPM, e.g., refs. 72–74) predictions for two specific epochs (in the beginning of the second and third visibility window) (Fig. 7, middle and right side). Both model concepts produce very similar fluxes due to the object's fast rotation. However, in the case of the TPM, the calculations depend on the selected spin-pole and thermal properties. Here, we used the non-convex model #1 with spin pole $(\lambda, \beta) = (36°, -44°)$, a rotation period of 5.35 min, and a range of thermal properties.

Figure 7 (left) shows the long-term flux predictions in μJy (different colours for the different MIRI bands). The flux changes are caused by the rapidly changing distances (with maxima at the shortest JWST-1998 KY_{26} distance) and phase angle. The overall flux level is driven by the object's size (here, we assumed an effective diameter of 11 m), the albedo has only a minor influence on the predictions. The times with JWST visibility are indicated by the thick blue and red lines. Due to its proximity to the Sun, 1998 KY_{26} cannot be observed by JWST between March 2025 and November 2027. We excluded the first visibility window (mid-Nov 2027 to late Jan 2028) due to the object's location inside the micro-meteoroid avoidance zone (MMAZ), where observations are not recommended[75]. In addition, 1998 KY_{26} is expected to be faint (JWST-centric distance is larger than 0.55 au). Within the remaining two visibility windows, we looked at possible MIRI imager measurements in late March 2028 with 1998 KY_{26} seen at a low phase angle of about 35° and in the beginning of October 2028 with a phase angle of about 73°. Both epochs represent moments where the object has its maximum brightness within the given visibility window. The two figures (Fig. 7, middle, right side) show TPM predictions for a wide range of thermal inertia (30, 100, and 500 J m^{-2} K^{-1} $s^{-1/2}$), assuming a size of 30 m with an albedo of $p_V = 0.12$ (solution given in ref.[6]), shown in blue, and our solution with $D = 11$ m, $p_V = 0.58$, shown in red. In both cases we used the abovementioned spin properties and a low level of surface roughness. The horizontal black lines indicate the calculated MIRI S/N = 10 flux limits[76], assuming a medium sky background level and 30-min integration time per filter. The calculations show that the intermediate MIRI bands (F770W to F1500W) would allow good detections (i) to test our size estimate and (ii) to constrain the object's thermal properties. Due to the low flux levels and the required long integration times (longer than the object's rotation period), it will not be possible to measure a thermal lightcurve. The MIRI measurements would be the only feasible option to verify our finding of a much smaller effective size (in comparison to the published value[6]) before the Hayabusa2# rendezvous in July 2031. In addition, the measurements would put strong constraints on the object's thermal properties.

https://doi.org/10.1038/s41467-025-63697-4

Table 2 | Best-fit orbital elements at epoch JD 2459059.5 (2020 Jul 29.0 TDB)

Element	Value	Uncertainty (1σ)
Eccentricity, e	0.2018782081	7.35×10^{-8}
Perihelion distance, q [au]	0.9839821759	5.10×10^{-8}
Time of perihelion, T_p [JD TDB]	2459001.1836694	1.21×10^{-5}
Longitude of ascending node, Ω [deg]	84.3669158	1.81×10^{-5}
Argument of perihelion, ω [deg]	209.3725241	1.97×10^{-5}
Inclination, i [deg]	1.48101564	1.55×10^{-6}

Values are given with 1σ formal uncertainties.

Astrometry and non-gravitational forces

In order to constrain the orbital behaviour of the object as accurately as possible, we took advantage of the imaging detections obtained for lightcurve purposes to also extract high-precision astrometric measurements of the object. For each telescope, and each observing night, we extracted between 2 and 8 astrometric positions, depending on the temporal arc of each dataset and the SNR of the object in the frames. This effort produced 8 high-precision astrometric tracklets for 1998 KY_{26}: 4 from GTC data, 2 from VLT data, and one each from the Blanco telescope and from Southern African Large Telescope (this dataset was only used for astrometric purposes, since it did not achieve a sufficient signal-to-noise ratio for physical characterisation; it is therefore not mentioned in other sections of this work). All measurements were obtained using the Gaia mission's second data release (Gaia DR2) catalogue as reference, and taking the proper motion of each field star into account. For each measurement, we also computed formal astrometric uncertainties, essential to evaluate how well an orbit solution fits the available data. Some of the detections were sufficient to extract measurements with error bars below 30 mas.

Similar astrometric procedures were also applied to earlier detections of 1998 KY_{26} from VLT and Subaru, collected during the 2020 apparition. These additional astrometric points are useful to further constrain the trajectory in a separate earlier apparition, putting additional constraints on the dynamical model.

Modelling the trajectory of 1998 KY_{26} presents significant challenges. Astrometric data collected during the 2020 apparition already required the inclusion of an out-of-plane non-gravitational acceleration seemingly incompatible with radiation forces perturbing the motion of asteroids[10]. The 2024 astrometry further complicates the situation and even the out-of-plane acceleration fails to adequately reproduce the trajectory as constrained by observational data.

Given the constraints on the rotation state derived in this paper, we opted for a non-gravitational-acceleration model combining solar radiation pressure and the Yarkovsky effect, with radial and transverse terms[77], and a polar acceleration based on the seasonally varying outgassing model[21]:

$$\mathbf{a}_{NG} = \left(\frac{1\,\mathrm{au}}{r}\right)^2 \left(A_1\hat{\mathbf{r}} + A_2\hat{\mathbf{t}} + C_0(\hat{\mathbf{r}}\cdot\hat{\mathbf{s}})\hat{\mathbf{s}}\right) \quad (5)$$

where r is the heliocentric distance, $\hat{\mathbf{r}}$ and $\hat{\mathbf{t}}$ are the orbital radial and transverse directions, $\hat{\mathbf{s}}$ is the spin's north pole direction, and A_1, A_2, and $C_0 > 0$ parametrize the acceleration. With this model, we attempted to fit the entire observation arc from 1998 to 2024. The weighted RMS of the best-fit solution is 0.437, and the resulting orbital elements are presented in Table 2.

Because of the sensitivity of this model on the spin pole, we investigated the possibility that the astrometry could provide independent constraints on the spin orientation. We scanned a raster in the pole's ecliptic longitude and latitude, and for each point, we estimated A_1, A_2, and C_0 from the orbital fit. Figure 8 shows the χ^2 of the fit as a function of the pole orientation compared to the pole solutions from the SAGE modelling technique (Table 1). There are two χ^2 minima for antipodal orientations due to the symmetry of the seasonal outgassing model. Interestingly, three of the pole solutions from physical characterisation are not compatible with our non-gravitational acceleration model because they correspond to non-physical, negative values of C_0. On the other hand, the remaining pole solution, which happens to be the favoured one from physical characterisation, is very close to one of the two minima with $\Delta\chi^2 = 1$. If we assume P_1 in the non-gravitational acceleration model, we find $A_2 = (-21.0 \pm 0.8) \times 10^{-14}$ au/d^2. For the Yarkovsky effect, a negative A_2 requires a retrograde rotation[78], which is consistent with P_1. While the mechanism triggering non-gravitational accelerations on KY is not yet fully understood, under the assumptions of the model adopted in this paper, there is a clear preference for pole solution P_1 from the orbital motion of the asteroid.

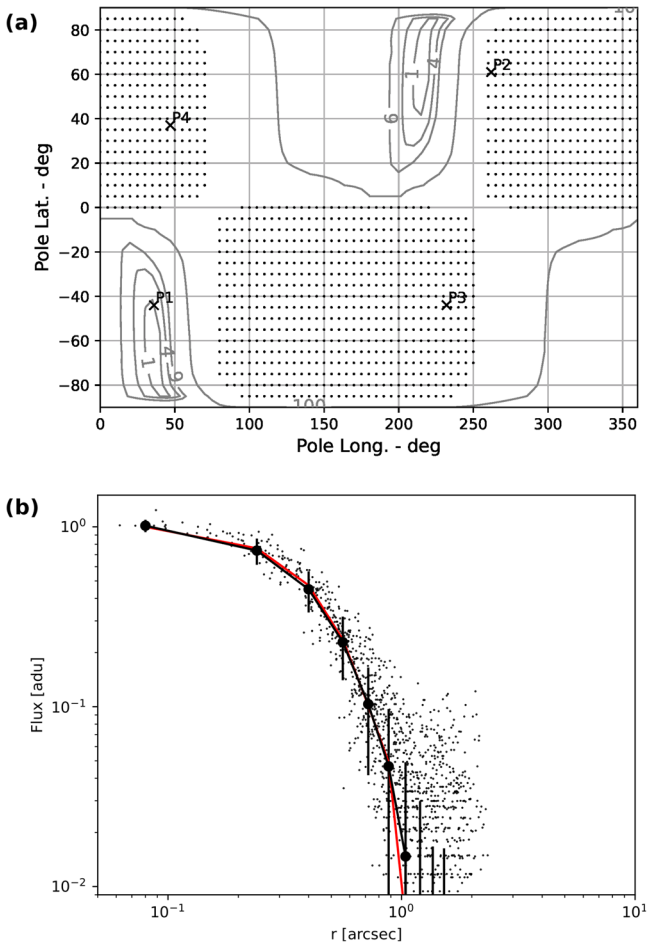

Fig. 8 | Search for potential activity. a Raster plot in ecliptic coordinates (longitude λ, latitude β) showing the spin-axis orientation search space. Contour lines represent the χ^2 values of the model fit to optical and radar astrometry, relative to the minimum. The global minimum is located at (λ, β) = (215°, + 60°), with an antipodal solution at (35°, − 60°). Black dots indicate grid points where the derived dynamical parameter C_0 is non-physical ($C_0 < 0$) and should be excluded. Crosses mark the four spin-axis solutions obtained from lightcurve inversion using the SAGE modeling technique. **b** Profile of 1998 KY_{26} extracted from the superstack image obtained with Gemini observations on 31 May 2024. Small dots represent individual pixels; black line and circles, the average profile; the red line is the scaled average profile of several field stars. The fluxes are in detector units. Vertical error bars represent the 1σ uncertainties in the measured flux, in analogue-to-digital units (ADU). The profile emphasizes the high signal-to-noise region (0-1 arcsec) and includes a portion of the lower signal-to-noise regime (1–2 arcsec) for context.

Search for resolved dust

The individual images are stacked in two steps: first, centred on the object and, second, aligned to the background stars. A radial profile is extracted for each object stack, and a reference profile is obtained from a few well-exposed stars near the object's position in the background stack. To build the average profile, we bin the sky-subtracted flux of pixels in annuli centred on the target, while also keeping track of the dispersion and the number of contributing pixels.

For the star profile, non-sidereal guiding may introduce slight elongation of the stellar images. In this case, only the pixels in the direction perpendicular to the elongation are used to accurately reflect the point-spread function. The stellar profile is then scaled to match the object profile. Frames where stellar images are not point sources, or where they appear as elongated point sources (likely due to guiding issues or variable extinction), were excluded from the analysis.

Figure 8 displays the individual pixels, the average object profile, and the reference stellar profile for comparison. In these profiles, a dust coma would appear as an excess of the object profile over the stellar profile. However, none of the profiles show such an excess; in all cases, the stellar profile is well within the error bars of the object profile, indicating no dust has been detected.

Two methods are used to quantify this non-detection:

- One method assumes that the maximum dust content in the inner profile is constrained by its error bars.
- The other method uses the noise in the outer profile (where the object profile fades into the sky background noise) to set an upper limit for the dust content.

These two sources of noise are measured, their corresponding fluxes are converted into a number of dust grains (considering a radius $a = 1\,\mu m$, cometary albedo $p = 0.5$) which is then converted in a mass (with a density $\rho = 3.5\ g\ cm^{-3}$).

Supplementary Table 4 lists these masses for the various stacks. These 1 σ limits are in the range 0.005–0.06 kg. A 5-σ excess would be clearly visible, either on the inner or outer profile, so the quantity of dust around the object is less than 0.03–0.3 kg in the form of 1-micron dust grains, ruling out cometary activity. Larger pebbles would result in a higher mass. For example, 1-mm grains would lead to an equivalent mass limit of 100–500 kg. Additionally, this method is not sensitive to pebbles very close to the object, as their corresponding dust cloud would not be resolved. Supplementary Table 4 presents 1-σ limits on the resolved dust mass: V is the magnitude of the object; mag_{dust} is the 1 σ maximum magnitude contribution from the dust. The maximum dust contribution is converted into the number of grains n_{grains}, and a mass m_{grains}, where $grain_a = 1.0 \times 10^{-6}$ m, $grain_p = 0.5$, $grain_\rho = 3.5$ g/cm^3, and $grain_m = 1.47 \times 10^{-14}$ kg. The inner profile is from 0.05" to 1", and the outer profile ranges from 1.5" to 2", where the object profile fades into the sky noise.

Data availability

DECam data are available from the NOIRLab Astro Data archive (https://astroarchive.noirlab.edu), under PropID 2024A-786651. Gemini GMOS data are available from the Gemini Observatory Archive (https://archive.gemini.edu), under PropID GS-2024A-DD-107. OSIRIS+/GTC data is available from the GTC Public Archive at CAB (INTA-CSIC) (https://gtc.sdc.cab.inta-csic.es/gtc/index.jsp) under PropIDs GTC05-24ADDT and GTC03-24BDDT. The radar data is available upon request. SALT data is available from the SAAO/SALT Data Archive (https://ssda.saao.ac.za/), under Proposal Code 2024-1-DDT-003. Optical astrometry is publicly available from the Minor Planet Centre (https://www.minorplanetcenter.net/db_search/show_object?utf8=%E2%9C%93&object_id=1998+KY26) and the radar astrometry is publicly available from the Solar System Dynamics Group at the Jet Propulsion Laboratory (https://ssd.jpl.nasa.gov/tools/sbdb_lookup.html#/?sstr=1998%20KY26&view=OPR). VLT data are available from the ESO Science Archive (https://archive.eso.org) under programme ID 114.26ZC.001. The datasets generated during and/or analysed during the current study are available from the corresponding author upon request. The photometric data generated in this study are provided in the Source Data file and are listed in Table 1 and Table 2 of the Supplementary Information. Source data are provided with this paper.

Code availability

The SAGE shape modelling code[12] was used to invert the lightcurve data and to constrain rotation periods, pole orientations, and non-convex shapes. The convex lightcurve inversion code[13,46–48] was used to derive rotation periods, pole orientations, convex shapes, and absolute magnitudes. The SHAPE radar modelling code was employed for radar data interpretation; although there is no dedicated publication describing this software, its methodology and applications are documented in Magri et al.[55]. The code is available upon request from the developers. The JET PROPULSION LABORATORY COMET AND ASTEROID ORBIT DETERMINATION PACKAGE (ODP) was used to analyse orbital evolution and non-gravitational perturbations; while there is no stand-alone code reference, its methodologies and applications are described in Farnocchia et al.[77]. The finite-element modelling (FEM) approach uses a code developed by M.H. to quantify the dynamical variation in stress fields[56]. All proprietary codes and tools developed by the authors and used in this study are available from the corresponding author for academic research purposes under a collaboration agreement. The TYCHO TRACKER software[79] is publicly available at https://www.tycho-tracker.com/.

References

1. Watanabe, S. et al. Hayabusa2 arrives at the carbonaceous asteroid 162173 Ryugu—a spinning top-shaped rubble pile. *Science* **364**, 268–272 (2019).
2. Lauretta, D. S. et al. The unexpected surface of asteroid (101955) Bennu. *Nature* **568**, 55–60 (2019).
3. Burdanov, A. Y. et al. JWST sighting of decameter main-belt asteroids and view on meteorite sources. *Nature* **1476**, 37–51 (2024).
4. Kikuchi, S. et al. Preliminary design of the Hayabusa2 extended mission to the fast-rotating asteroid 1998 KY26. *Acta Astron.* **211**, 295–315 (2023).
5. MPEC 1998-L02 KY26. https://www.minorplanetcenter.net/mpec/J98/J98L02.html (1998).
6. Ostro, S. J. et al. Radar and optical observations of asteroid 1998 KY26. *Science* **285**, 557–559 (1999).
7. Devogèle, M. et al. Aperture photometry on asteroid trails: Detection of the fastest-rotating near-Earth object. *Astron. Astrophys.* **689**, A211 (2024).
8. Carbognani, A., Fenucci, M., Salerno, R. & Micheli, M. Ab initio strewn field for small asteroids impacts. *Icarus* **425**, 116345 (2025).
9. Taylor, A. G. et al. The dynamical origins of the dark comets and a proposed evolutionary track. *Icarus* **420**, 116207 (2024).
10. Seligman, D. Z. et al. Dark Comets? Unexpectedly large non-gravitational accelerations on a sample of small asteroids. *Planet. Sci. J.* **4**, 35 (2023).
11. Yamada, M. et al. Inflight calibration of the optical navigation camera for the extended mission phase of Hayabusa2. *Earth, Planets Space* **75**, 36 (2023).
12. Bartczak, P. & Dudziński, G. Shaping asteroid models using genetic evolution (SAGE). *Mon. Not. R. Astron. Soc.* **473**, 5050–5065 (2018).
13. Muinonen, K., Torppa, J., Wang, X. B., Cellino, A. & Penttilä, A. Asteroid lightcurve inversion with Bayesian inference. *Astron. Astrophys.* **642**, A138 (2020).
14. Marciniak, A. & Michałowski, T. Asteroids' spin axis distribution*. *AA* **512**, A56 (2010).
15. Muinonen, K. et al. A three-parameter magnitude phase function for asteroids. *Icarus* **209**, 542–555 (2010).

16. Gaffey, M. J., Reed, K. L. & Kelley, M. S. Relationship of E-type Apollo asteroid 3103 (1982 BB) to the enstatite achondrite meteorites and the Hungaria asteroids. *Icarus* **100**, 95–109 (1992).
17. Keil, K. Enstatite achondrite meteorites (aubrites) and the histories of their asteroidal parent bodies. *Geochemistry* **70**, 295–317 (2010).
18. Muinonen, K., Piironen, J., Shkuratov, Y. G., Ovcharenko, A. & Clark, B. E. Asteroid photometric and polarimetric phase effects. In *Asteroids III* (eds Bottke, Jr, W. F., Cellino, A., Paolicchi, P. & Binzel, R. P.) 123–138 (2002).
19. Rivera-Valentín, E. G. et al. Radar circular polarization ratio of near-earth asteroids: links to spectral taxonomy and surface processes. *Planet. Sci. J.* **5**, 232 (2024).
20. Shevchenko, V., Krugly, Y., Chiorny, V., Belskaya, I. & Gaftonyuk, N. Rotation and photometric properties of e-type asteroids. *Planet. Space Sci.* **51**, 525–532 (2003).
21. Taylor, A. G. et al. Seasonally varying outgassing as an explanation for dark comet accelerations. *Icarus* **408**, 115822 (2024).
22. Hirabayashi, M. & Scheeres, D. J. Stress and failure analysis of rapidly rotating asteroid (29075) 1950 DA. *Astrophys. J. Lett.* **798**, L8 (2014).
23. Hirabayashi, M. et al. Fission and reconfiguration of bilobate comets as revealed by 67P/Churyumov–Gerasimenko. *Nature* **534**, 352–355 (2016).
24. Beniyama, J. et al. Size constraint on Hayabusa2 extended mission rendezvous target 1998 KY_{26} via VLT/VISIR nondetection. *Astron. J.* **169**, 264 (2025).
25. Benner, L. A. M., Busch, M. W., Giorgini, J. D., Taylor, P. A. & Margot, J. L. Radar observations of near-earth and main-belt asteroids. In *Asteroids IV* (eds Michel, P., DeMeo, F. E. & Bottke, W. F.) 165–182 (2015).
26. Barnouin, O. S. et al. Shape of (101955) Bennu indicative of a rubble pile with internal stiffness. *Nat. Geosci.* **12**, 247–252 (2019).
27. Seligman, D. Z. et al. Two distinct populations of dark comets delineated by orbits and sizes. *Proc. Natl. Acad. Sci. USA* **121**, e2406424121 (2024).
28. Rozitis, B., MacLennan, E. & Emery, J. P. Cohesive forces prevent the rotational breakup of rubble-pile asteroid (29075) 1950 DA. *Nature* **512**, 174–176 (2014).
29. Hirabayashi, M., Scheeres, D. J., Sánchez, D. P. & Gabriel, T. Constraints on the physical properties of main belt comet P/2013 R3 from its breakup event. *Astrophys. J. Lett.* **789**, L12 (2014).
30. Scheeres, D., Hartzell, C., Sánchez, P. & Swift, M. Scaling forces to asteroid surfaces: the role of cohesion. *Icarus* **210**, 968–984 (2010).
31. Sánchez, P. & Scheeres, D. J. The strength of regolith and rubble pile asteroids. *Meteorit. Planet. Sci.* **49**, 788–811 (2014).
32. Brisset, J. et al. Asteroid regolith strength: role of grain size and surface properties. *Planet. Space Sci.* **220**, 105533 (2022).
33. Burdanov, A. Y. et al. JWST sighting of decameter main-belt asteroids and view on meteorite sources. *Nature* **638**, 74–78 (2024).
34. Kadono, T., Arakawa, M., Ito, T. & Ohtsuki, K. Spin rates of fast-rotating asteroids and fragments in impact disruption. *Icarus* **200**, 694–697 (2009).
35. Ormö, J. et al. Boulder exhumation and segregation by impacts on rubble-pile asteroids. *Earth Planet. Sci. Lett.* **594**, 117713 (2022).
36. Bottke, W. F., Vokrouhlický, D., Rubincam, D. P. & Nesvorný, D. The Yarkovsky and Yorp effects: implications for asteroid dynamics. *Annu. Rev. Earth Planet. Sci.* **34**, 157–191 (2006).
37. Brown, P., Spalding, R. E., ReVelle, D. O., Tagliaferri, E. & Worden, S. P. The flux of small near-Earth objects colliding with the Earth. *Nature* **420**, 294–296 (2002).
38. National Academies of Sciences, Engineering, and Medicine. *Origins, Worlds, and Life: A Decadal Strategy for Planetary Science and Astrobiology 2023-2032* (The National Academies Press, Washington, DC, 2022).
39. SAUSERO education software for the broad band imaging mode of OSIRIS+ at GTC, version 1.0.0. https://pypi.org/project/sausero/
40. Hirst, P. & Cardenes, R. A New Data Archive for Gemini - Fast, Cheap and in the Cloud. In Lorente, N. P. F., Shortridge, K. & Wayth, R. (eds.) *Astronomical Data Analysis Software and Systems XXV*, vol. 512 of *Astronomical Society of the Pacific Conference Series*, 53 (2017).
41. Labrie, K. et al. DRAGONS-a quick overview. *Res. Notes Am. Astron. Soc.* **7**, 214 (2023).
42. Simpson, C. et al. Dragons https://doi.org/10.5281/zenodo.10841622 (2024).
43. Manset, N. & Forshay, P. (eds.). *Astronomical Data Analysis Softward and Systems XXIII*, vol. 485 of *Astronomical Society of the Pacific Conference Series* (2014).
44. Ivezić, Ž. et al. Solar system objects observed in the Sloan Digital Sky Survey commissioning data. *Astron. J.* **122**, 2749 (2001).
45. DeMeo, F. & Carry, B. The taxonomic distribution of asteroids from multi-filter all-sky photometric surveys. *Icarus* **226**, 723–741 (2013).
46. Kaasalainen, M. & Torppa, J. Optimization methods for asteroid lightcurve inversion. I. Shape determination. *Icarus* **153**, 24–36 (2001).
47. Kaasalainen, M., Torppa, J. & Muinonen, K. Optimization methods for asteroid lightcurve inversion. II. The complete inverse problem. *Icarus* **153**, 37–51 (2001).
48. Muinonen, K. et al. Asteroid photometric phase functions from Bayesian lightcurve inversion. *Front. Astron. Space Sci.* **9**, 821125 (2022).
49. Virkki, A. K. et al. Arecibo planetary radar observations of near-earth asteroids: 2017 December-2019 December. *Planet. Sci. J.* **3**, 222 (2022).
50. Virkki, A. K. & Bhiravarasu, S. S. Modeling radar albedos of laboratory-characterized particles: application to the lunar surface. *J. Geophys. Res. (Planets)* **124**, 3025–3040 (2019).
51. Kaasalainen, M. & Lamberg, L. Inverse problems of generalized projection operators. *Inverse Probl.* **22**, 749–769 (2006).
52. Bartczak, P. & Dudziński, G. Volume uncertainty assessment method of asteroid models from disc-integrated visual photometry. *Mon. Not. R. Astron. Soc.* **485**, 2431–2446 (2019).
53. Ostro, S. J. Planetary radar astronomy. *Rev. Mod. Phys.* **65**, 1235–1279 (1993).
54. Hudson, R. S., Ostro, S. J. & Scheeres, D. J. High-resolution model of Asteroid 4179 Toutatis. *Icarus* **161**, 346–355 (2003).
55. Magri, C. et al. Radar observations and a physical model of Asteroid 1580 Betulia. *Icarus* **186**, 152–177 (2007).
56. Hirabayashi, M., Kim, Y. & Brozović, M. Finite element modeling to characterize the stress evolution in asteroid (99942) Apophis during the 2029 Earth encounter. *Icarus* **365**, 114493 (2021).
57. Hirabayashi, M., Sánchez, D. P. & Scheeres, D. J. Internal Structure of Asteroids Having Surface Shedding Due To Rotational Instability. *Astrophys. J.* **808**, 63 (2015).
58. Hirabayashi, M. Failure modes and conditions of a cohesive, spherical body due to YORP spin-up. *Monthly Not. R. Astron. Soc.* **454**, 2249–2257 (2015).
59. Hirabayashi, M. et al. Spin-driven evolution of asteroids' top-shapes at fast and slow spins seen from (101955) Bennu and (162173) Ryugu. *Icarus* **352**, 113946 (2020).
60. Hirabayashi, M. et al. Double asteroid redirection test (DART): structural and dynamic interactions between asteroidal elements of binary asteroid (65803) Didymos. *Planet. Sci. J.* **3**, 140 (2022).
61. Nakano, R. & Hirabayashi, M. Mass-shedding activities of asteroid (3200) Phaethon enhanced by its rotation. *Astrophys. J. Lett.* **892**, L22 (2020).
62. Cignoni, P. et al. MeshLab: an Open-Source Mesh Processing Tool. In *Eurographics Italian Chapter Conference* (eds Scarano, V., Chiara, R. D. & Erra, U.)(The Eurographics Association, 2008).

63. Si, H. TetGen, a Delaunay-Based Quality Tetrahedral Mesh Generator. *ACM Trans. Math. Softw.* **41**, 11 (2015).
64. Chen, W.-F., Han, D.-J. & Han, D.-J. *Plasticity for Structural Engineers* (J. Ross Publishing, 2007).
65. Macke, R. J., Consolmagno, G. J., Britt, D. T. & Hutson, M. L. Enstatite chondrite density, magnetic susceptibility, and porosity. *Meteorit. Planet. Sci.* **45**, 1513–1526 (2010).
66. DeMeo, F. E., Binzel, R. P., Slivan, S. M. & Bus, S. J. An extension of the Bus asteroid taxonomy into the near-infrared. *Icarus* **202**, 160–180 (2009).
67. Fornasier, S., Migliorini, A., Dotto, E. & Barucci, M. Visible and near infrared spectroscopic investigation of E-type asteroids, including 2867 Steins, a target of the Rosetta mission. *Icarus* **196**, 119–134 (2008).
68. Ćuk, M., Gladman, B. J. & Nesvorný, D. Hungaria asteroid family as the source of aubrite meteorites. *Icarus* **239**, 154–159 (2014).
69. Müller, T. G. et al. Asteroids seen by JWST-MIRI: Radiometric size, distance, and orbit constraints. *Astron. Astrophys.* **670**, A53 (2023).
70. Rivkin, A. S. et al. JWST Observations of Potentially Hazardous Asteroid 2024 YR4. *Res. Notes Am. Astron. Soc.* **9**, 70 (2025).
71. Lebofsky, L. A. & Spencer, J. R. Radiometry and thermal modeling of asteroids. In *Asteroids II* (eds Binzel, R. P., Gehrels, T. & Matthews, M. S.) 128–147 (1989).
72. Lagerros, J. S. V. Thermal physics of asteroids. I. Effects of shape, heat conduction and beaming. *Astron. Astrophys.* **310**, 1011–1020 (1996).
73. Lagerros, J. S. V. Thermal physics of asteroids. IV. Thermal infrared beaming. *Astron. Astrophys.* **332**, 1123–1132 (1998).
74. Müller, T. G. Thermophysical analysis of infrared observations of asteroids. *Meteorit. Planet. Sci.* **37**, 1919–1928 (2002).
75. JWST documentation: Micrometeoroid avoidance zone policies and procedures. https://jwst-docs.stsci.edu/jwst-opportunities-and-policies/jwst-general-science-policies/micrometeoroid-avoidance-zone-policies-and-procedures.
76. JWST exposure time calculator, version 4.0. https://jwst.etc.stsci.edu/.
77. Farnocchia, D., Chesley, S. R., Milani, A., Gronchi, G. F. & Chodas, P. W. Orbits, long-term predictions, impact monitoring. In *Asteroids IV* (eds Michel, P., DeMeo, F. E. & Bottke, W. F.) 815–834 (University of Arizona Press, 2015).
78. Farnocchia, D. et al. Near Earth Asteroids with measurable Yarkovsky effect. *Icarus* **224**, 1–13 (2013).
79. Parrott, D. Tycho tracker: a new tool to facilitate the discovery and recovery of asteroids using synthetic tracking and modern GPU hardware. *9th Annual Conference of the Society for Astronomical Sciences* Vol. **48**, 262 (2020).

Acknowledgements

TSR acknowledges funding from Ministerio de Ciencia e Innovación (Spanish Government), PGC2021, PID2021-125883NB-C21. This work was (partially) supported by the Spanish MICIN/AEI/10.13039/501100011033 and by "ERDF A way of making Europe" by the "European Union" through grant PID2021-122842OB-C21, and the Institute of Cosmos Sciences University of Barcelona (ICCUB, Unidad de Excelencia 'María de Maeztu') through grant CEX2019-000918-M. PB acknowledges funding through the Spanish Government retraining plan 'María Zambrano 2021-2023' at the University of Alicante (ZAMBRANO22-04). DO was supported from grant nr 2022/45/B/ST9/00267 from National Science Centre, Poland. Research by KM has been supported by Research Council of Finland grants 336546, 345115, and 359893. AKV was supported by Research Council of Finland grant 347627. This project used data obtained with the Dark Energy Camera (DECam), which was constructed by the Dark Energy Survey (DES) collaboration. Funding for the DES Projects has been provided by the DOE and NSF (USA), MISE (Spain), STFC (UK), HEFCE (UK), NCSA (UIUC), KICP (U. Chicago), CCAPP (Ohio State), MIFPA (Texas A&M), CNPQ, FAPERJ, FINEP (Brazil), MINECO (Spain), DFG (Germany) and the Collaborating Institutions in the Dark Energy Survey, which are Argonne Lab, UC Santa Cruz, University of Cambridge, CIEMAT-Madrid, University of Chicago, University College London, DES-Brazil Consortium, University of Edinburgh, ETH Zürich, Fermilab, University of Illinois, ICE (IEEC-CSIC), IFAE Barcelona, Lawrence Berkeley Lab, LMU München and the associated Excellence Cluster Universe, University of Michigan, NOIRLab, University of Nottingham, Ohio State University, OzDES Membership Consortium, University of Pennsylvania, University of Portsmouth, SLAC National Lab, Stanford University, University of Sussex, and Texas A&M University. Based on observations at Cerro Tololo Inter-American Observatory at NSF's NOIRLab (NOIRLab Prop. ID 2024A-786651; PI: T. Santana-Ros), which is managed by the Association of Universities for Research in Astronomy (AURA) under a cooperative agreement with the National Science Foundation. Based on observations made with the Gran Telescopio Canarias (GTC), installed at the Spanish Observatorio del Roque de los Muchachos of the Instituto de Astrofísica de Canarias, on the island of La Palma. Some of the observations reported in this paper were obtained with the Southern African Large Telescope (SALT). Polish participation in SALT is funded by grant No. MEiN nr 2021/WK/01. Based on observations collected at the European Southern Observatory under ESO programme 114.26ZC.001. Part of this research was conducted at the Jet Propulsion Laboratory, California Institute of Technology, under a contract with the National Aeronautics and Space Administration (80NM0018D0004). AR and REC acknowledge support from the UK Science and Technology Facilities Council. Based on observations made at the international Gemini Observatory, a programme of NSF NOIRLab, is managed by the Association of Universities for Research in Astronomy (AURA) under a cooperative agreement with the U.S. National Science Foundation on behalf of the Gemini partnership: the U.S. National Science Foundation (United States), the National Research Council (Canada), Agencia Nacional de Investigación y Desarrollo (Chile), Ministerio de Ciencia, Tecnología e Innovación (Argentina), Ministério da Ciência, Tecnologia, Inovações e Comunicações (Brazil), and Korea Astronomy and Space Science Institute (Republic of Korea). Part of this research was carried out at the Jet Propulsion Laboratory, California Institute of Technology, under a contract with the National Aeronautics and Space Administration (NASA). This material is based in part upon work supported by NASA under the Science Mission Directorate Research and Analysis Programmes. GTC Public Archive is developed in the framework of the Spanish Virtual Observatory project supported by the Spanish MINECO through grants AYA 2011-24052 and AYA 2014-55216.

Author contributions

T.S.-R. led the photometric observation campaign, performed the photometric measurements and participated in all aspects of the discussion and in the paper writing; P.B. produced the non-convex model with the SAGE inversion method, calculated the colours and participated in the discussion; K.M. produced the convex modelling, studied the phase curve, absolute magnitude, and geometric albedo, and participated in the discussion; A.R. and R.E.C. reprocessed the radar data, provided the size estimate and participated in the discussion; T.M. provided the predictions for JWST-MIRI visibility windows and participated in the discussion; M.H. investigated the internal structure and participated in the discussion; D.F. analysed the orbit and non-gravitational perturbations; M.M. performed the astrometric measurements; M.B. and L.A.M.B. helped with the interpretation of the reprocessed radar data; O.H. performed the search for resolved dust; D.O. participated in the discussion of the object's taxonomy; A.K.V. participated in the interpretation of the radar circular-polarisation ratio; A.C.B. and P.G.B. participated in the discussion of the internal structure and the possible origin of the object; C.E.M.-V. coordinated the observations obtained at Gemini South and helped with the GMOS

data reduction; A.C.-L. obtained the GTC observations and reduced the data; K.V. obtained the observations with Blanco-DECam;

Competing interests
The authors declare no competing interests.

Additional information
Supplementary information The online version contains supplementary material available at https://doi.org/10.1038/s41467-025-63697-4.

Correspondence and requests for materials should be addressed to T. Santana-Ros.

Peer review information *Nature Communications* thanks the anonymous reviewers for their contribution to the peer review of this work. A peer review file is available.

[1]Departamento de Física, Ingeniería de Sistemas y Teoría de la Señal, Universidad de Alicante, San Vicente del Raspeig, Alicante, Spain. [2]Institut de Ciències del Cosmos (ICCUB), Universitat de Barcelona (UB), Barcelona, Spain. [3]Instituto Universitario de Física Aplicada a las Ciencias y a las Tecnologías, Universidad de Alicante, Alicante, Spain. [4]Astronomical Observatory Institute, Faculty of Physics and Astronomy, A. Mickiewicz University, Poznań, Poland. [5]Department of Physics, University of Helsinki, Helsinki, Finland. [6]Institute for Astronomy, University of Edinburgh, Royal Observatory, Edinburgh, UK. [7]Max-Planck-Institut für extraterrestrische Physik, Garching, Germany. [8]Georgia Institute of Technology, Atlanta, GA, USA. [9]Jet Propulsion Laboratory, California Institute of Technology, Pasadena, CA, USA. [10]ESA NEO Coordination Centre, Planetary Defence Office, Frascati (RM), Italy. [11]European Southern Observatory, Garching-bei-München, Germany. [12]GRANTECAN, La Palma, Spain. [13]Instituto de Astrofísica de Canarias, La Laguna, Tenerife, Spain. [14]International Gemini Observatory/NSF NOIRLab, Hilo, HI, USA. [15]Cerro Tololo Inter-American Observatory/NSF NOIRLab, La Serena, Chile. ✉e-mail: tsantanaros@icc.ub.edu